

# Measurement of directional muon beams generated at the Berkeley Lab Laser Accelerator

Davide Terzani,<sup>1,\*</sup> Stanimir Kisyov,<sup>1</sup> Stephen Greenberg,<sup>1,2</sup> Luc Le Pottier,<sup>1,2</sup> Maria Mironova,<sup>1</sup> Alex Picksley,<sup>1</sup> Joshua Stackhouse,<sup>1,3</sup> Hai-En Tsai,<sup>1</sup> Raymond Li,<sup>1,3</sup> Ela Rockafellow,<sup>4</sup> Timon Heim,<sup>1</sup> Maurice Garcia-Sciveres,<sup>1</sup> Carlo Benedetti,<sup>1</sup> John Valentine,<sup>1</sup> Howard Milchberg,<sup>4</sup> Kei Nakamura,<sup>1</sup> Anthony J. Gonsalves,<sup>1</sup> Jeroen van Tilborg,<sup>1</sup> Carl B. Schroeder,<sup>1,3</sup> Eric Esarey,<sup>1</sup> and Cameron G. R. Geddes<sup>1</sup>

<sup>1</sup>*Lawrence Berkeley National Laboratory, Berkeley, CA 94720, USA*

<sup>2</sup>*Department of Physics, University of California, Berkeley, CA 94720, USA*

<sup>3</sup>*Department of Nuclear Engineering, University of California, Berkeley, CA 94720, USA*

<sup>4</sup>*University of Maryland, College Park, MD 20742, USA*

(Dated: November 5, 2024)

We present the detection of directional muon beams produced using a PW laser at the Lawrence Berkeley National Laboratory. The muon source is a multi-GeV electron beam generated in a 30 cm laser plasma accelerator interacting with a high- $Z$  converter target. The GeV photons resulting from the interaction are converted into a high-flux, directional muon beam via pair production. By employing scintillators to capture delayed events, we were able to identify the produced muons and characterize the source. Using theoretical knowledge of the muon production process combined with simulations that show outstanding agreement with the experiments, we demonstrate that the multi-GeV electron beams produce muon beams with GeV energies and fluxes, at a few meters from the source, up to 4 orders of magnitude higher than cosmic ray muons. Laser-plasma-accelerator-based muon sources can therefore enhance muon imaging applications thanks to their compactness, directionality, and high fluxes which reduce the exposure time by orders of magnitude compared to cosmic ray muons. Using the Geant4-based simulation code we developed to gain insight into the experimental results, we can design future experiments and applications based on LPA-generated muons.

## I. INTRODUCTION

Muons beams have attracted considerable attention in recent years because of their unique properties and potential applications across various fields of physics. However, production of muon beams for fundamental physics research, for instance a future TeV-class muon-muon collider [1] or the Muon  $g-2$  experiment at Fermilab [2], is challenging and it is currently done by accelerating high-energy proton beams in large-scale facilities, colliding them with fixed targets and collecting the created mesons that will eventually decay into muons [3].

Given the large size of the accelerators, proton-based muon production is not suitable for imaging applications because neither the source nor the typical imaging samples can be transported. In fact, thanks to their considerable penetration power, muons are used for non-destructive imaging of large or concealed objects [4], which must be performed on-site. For such reason, currently the only available source of muons for imaging applications are the cosmic rays, which, when interacting with the Earth's atmosphere, generate showers of particles, including muons, that are accessible in any unshielded place on the planet. The incoming muon flux on the Earth's surface can be approximated as  $dN/d\Omega dS dt \approx 70 \cos^2(\theta) \text{ m}^{-2} \text{ s}^{-1} \text{ sr}^{-1}$  [5], where  $\theta$  is the angle from the zenith, along which the flux is maximum. For most

of the imaging applications, such a muon flux requires months of exposure before a statistically significant signal is accumulated. For instance, when imaging objects along the horizontal axis, the muon flux is reduced to  $dN/dS dt \ll 0.1 - 1 \text{ m}^{-2} \text{ s}^{-1}$  due to the limited angular aperture of the detectors. Therefore, muography via cosmic ray muons can generally be applied only to objects that are immobile over long periods of time. A notable and fascinating example of their use was the discovery of a hidden chamber in Khufu's Pyramid (Great Pyramid of Giza) [6, 7]. They also enable investigating the magmatic chambers of active volcanoes [8], blast furnaces [9], and nuclear waste [10–12]. These are only a few examples of the available applications and implementations of the muography technique. For a more general review see Refs. [13, 14] and references therein.

Laser plasma accelerators (LPAs) provide an alternative source of muon beams as a byproducts of the collision of an LPA-generated electron beam with a high- $Z$  target [15], a possibility supported by some numerical studies [16, 17]. Several laboratories have demonstrated generation of 100s MeV to multi-GeV-class electron beams in targets up to tens of centimeters [18–27], providing enough energy for muon generation via pair-production. Pair-produced muons are very suitable for muography as they are characterized by high-energy, of the order of the initial electron energy, and low divergence and they are generated directly into the solid target where the interaction is taking place. Currently available LPAs, operating at repetition rates between 1 and 10 Hz, can generate directional muon fluxes up to four orders of magni-

\* dterzani@lbl.gov

tude higher than cosmic rays, thus providing substantial speedups to applications that typically require months of exposure times. A next generation kHz LPA [28] could further improve this factor by three orders of magnitude, opening new avenues to the use of muons in imaging large objects in only a few minutes. A LPA-based muon source provides the essential characteristics that are needed for imaging applications together with the advantages of a compact source that can, potentially, be deployed on the imaging site.

In this paper we present the generation and measurement of GeV muons using the BErkeley Laboratory Laser Accelerator (BELLA) Facility at the Lawrence Berkeley National Laboratory. In Sec. II we give an overview of the relevant muon production mechanisms, highlighting the characteristics of the generated muons. In Sec. III we present the setup for the electron beam generation and the production and measurements of muons. In Sec. IV we analyze the results of the experiments and show how muons are identified. We demonstrate that the electron beams interacting with the shielding configuration of our laboratory generate muons via different mechanism and that we can spatially separate them into a directional and a quasi-isotropic source. Simulations that reproduce the experimental measurements are presented in Sec. V, where we investigate in detail the muon production process in the experimental cave. We obtain an excellent agreement with the measured number of muons, demonstrating the fidelity of our tool. Sec. VI presents the conclusions of our work and the next steps.

## II. MECHANISMS OF MUON PRODUCTION IN HIGH- $Z$ MATERIALS

When a high-energy electron traveling in a solid converter target is deviated by an atomic nucleus, it emits high energy photons, or *Bremsstrahlung* radiation [29]. The energy distribution of the Bremsstrahlung photons is characterized by an exponential-like decay, extending to the same maximum energy as the initial electron [29, 30]. The angle of emission is confined within a cone of angular aperture  $\Delta\theta_B \simeq 1/\gamma_e$ , where  $\gamma_e$  is the Lorentz factor of the radiating electron. Bremsstrahlung photons which interact with the background atomic nuclei can be converted into pairs of charged leptons (a particle and an antiparticle) via the *Bethe-Heitler* process if their energy is  $E_\gamma \geq 2m_p c^2$ , where  $m_p$  is the lepton mass, and  $c$  the speed of light in vacuum. The cross-section for the Bethe-Heitler production is proportional to the inverse of the particle mass squared [31], i.e.,  $\sigma_{BH} \propto 1/m_p^2$ , and the generated particles are emitted along the photon propagation direction, thus resulting in a particle shower confined within an angle  $\lesssim \Delta\theta_B$ . The energy spectrum of the products follows the Bremsstrahlung distribution, with a maximum energy  $E_{max} = E_\gamma - 2m_p c^2$ , due to energy-momentum conservation. We note that such energy distribution cannot be modeled appropriately using

a relativistic Maxwellian distribution. In fact, there is no fundamental reason to support such modeling as the products of pair production that exit the target do not constitute a thermalized plasma. The concept of temperature in this context is ill-defined, as opposed to the Bremsstrahlung radiation emitted by a black body. Even though the exponential-like tail of the Bremsstrahlung distribution resembles a relativistic Maxwellian and one could interpret its slope as related to some temperature-like parameter, the peak energy of the Bremsstrahlung distribution strongly depends on the target design and the selection angle used to select the final particles because it is related, for instance, to the particle reabsorption into the target itself. Therefore, describing *a-priori* the energy spectrum of pair produced particles using a relativistic Maxwellian distribution of given temperature is not acceptable, as the temperature parameter does not have a physical meaning in this context and it is not related to the peak energy of the distribution of the pair-produced particles.

Given that  $e^+e^-$  pairs, i.e., positron-electron, are the most probable products of the Bethe-Heitler process, Bremsstrahlung radiation induced by the propagation of an electron beam into high- $Z$  targets (e.g., tungsten or lead) has been used as a source of positron beams for conventional acceleration for several decades [30] and it has been extensively investigated in experiments.

Both the Bremsstrahlung and the Bethe-Heitler emissions develop over a characteristic radiation length  $X_0$ . The radiation length is defined as the length over which an electron propagating in the material loses all but  $1/e$  of its initial energy, which corresponds to  $7/9$  of the mean free path for Bethe-Heitler emission. The value of  $X_0$  depends on the atomic composition of the material and on its density. For high- $Z$  materials, its value ranges from millimeters to centimeters [30].

The properties of photon decay into  $\mu^+\mu^-$  pairs are analogous to the  $e^+e^-$  pair creation, but the cross section is reduced by a factor  $R = m_e^2/m_\mu^2 = 2.34 \times 10^{-5}$ . For this reason, it has not been subject to the same detailed experimental investigations and applications.

In addition to the Bethe-Heitler mechanism, the interactions of electrons with targets also lead to the production of pions ( $\pi^\pm$ ) which subsequently decay into muons (with a lifetime  $\tau_{\pi^\pm} = 2.6 \times 10^{-8}$  s). In particular, main sources of pions in the material are the processes  $\gamma + p \rightarrow \pi^+ + n$ ,  $\gamma + n \rightarrow \pi^- + p$ , and  $\gamma + N \rightarrow \pi^+ + \pi^- + N$ , where the  $\gamma$  rays interacting with the background protons ( $p$ ), neutrons ( $n$ ), and nucleons ( $N = p, n$ ) are the ones produced via Bremsstrahlung [15]. Analogous processes apply to kaon creation, although with a lower probability due to the higher kaon mass. Both pions and kaons decay into muons, therefore we will refer to the muon flux resulting from this mechanism as coming from a more general meson decay. The total cross section for muon production through meson decay in a high- $Z$  target is higher than the one for the Bethe-Heitler  $\mu^+\mu^-$  process. However, given the large meson rescattering and absorp-

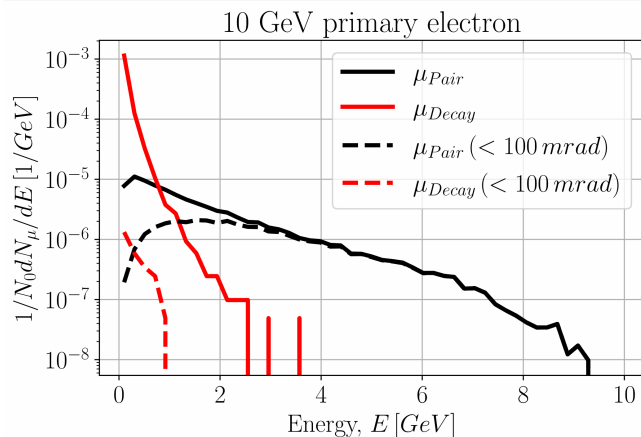


FIG. 1. Simulated energy spectra of muons generated via pair production and decay from a 10 GeV electron beam propagating in a 2.1 cm-thick tungsten target. The distributions are normalized per initial primary electron. The solid black and red lines correspond to the total yield of pair produced and decay muons, respectively. The dashed black and red lines presents the spectrum of respectively pair and decay produced muons within 100 mrad. Simulation results show that effectively all pair produced muons with  $E \simeq 4$  GeV are confined within 100 mrad.

tion cross sections, the resulting meson flux is weaker and not well collimated in a thick target [15]. Therefore, we expect some contributions to the number of muons from meson decay at large angles. Moreover, due to the relativistic dilation of the proper time, only low energy mesons decay in the vicinity of the converter, resulting in a sharp cut-off of the spectrum at high energies. It is possible to produce high energy muons via meson decay, but it requires  $\sim$ km-scale separations from the converter.

Fig. 1 shows simulated energy spectra, normalized per initial primary electron, of muons generated respectively via pair production and meson decay from a 10 GeV electron beam propagating in a 2.1 cm-thick tungsten target. The simulations were performed using the Geant4 toolkit for simulation of the propagation of particles through matter [32–34], including solely the monoenergetic electron beam and tungsten target in the setup geometry. The solid black line is the spectrum of muons generated via Bethe-Heitler integrated over  $4\pi$ , while the dashed black line is the spectrum of muons selected within a 100 mrad cone, which effectively contains all the muons produced with energies  $E \gtrsim 4$  GeV. The red line is the energy spectrum of muons generated via meson decay over the  $4\pi$  angle. Muons from meson decay are statistically insignificant within 100 mrad.

We show the effect of target thickness on the number of muons produced per initial electron in Fig. 2, with results from Geant4 simulations. The pair production only depends on the normalized thickness, i.e., the number of radiation lengths traversed, and does not show significant differences between different materials. The number of pair-produced muons is maximum between  $(6 - 10) X_0$

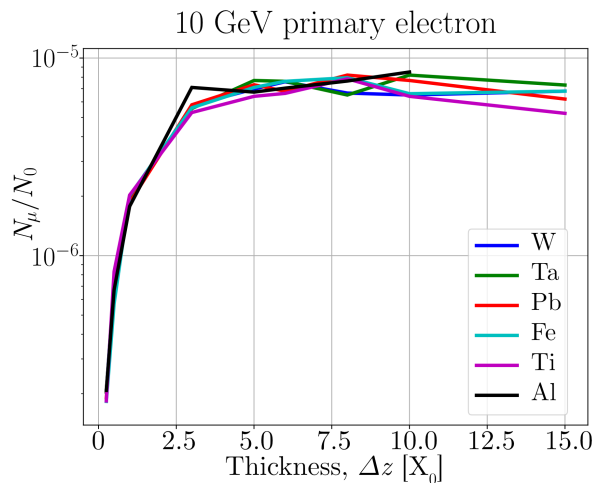


FIG. 2. Simulated yields of pair produced muons within 100 mrad along the primary 10 GeV electron beam axis for different materials and their thicknesses expressed in radiation lengths  $X_0$ . Normalization to a single primary electron is applied. The plot shows a saturation of the yield at  $\sim 6 X_0$  and independence of the target material.

for an initial 10 GeV electron beam, similarly to what is expected for positrons [30], and slowly decreases for larger thicknesses due to the high penetration power of muons.

In this section we reviewed different mechanisms for muon production, highlighting their characteristics. Pair production yields a directional and collimated muon beam, while meson decay generates a quasi-isotropic muon flux. In the next sections we will show how the interaction of an electron beam with the shielding configuration of our laboratory combines these processes. The electron beam dump suppresses the meson propagation, absorbing all but muon produced via pair production, while mesons are generated in other high- $Z$  elements along the beam path, which do not possess the same filtering power, and eventually decay into a quasi-isotropic background of low-energy muons.

### III. EXPERIMENTAL SETUP

We carried on an experimental campaign to generate and measure muons at the BELLA center between December 2023 and January 2024. The laser-plasma accelerator was driven using the BELLA PW laser [35]. A detailed description of the accelerator can be found in [27] and a schematic of the experiment can be found in Fig. 3. The drive laser duration was  $\sim 40$  fs and was focused to a spot-size of  $w_0 = (53 \pm 1) \mu\text{m}$ , at the entrance of a 30-cm-long hydrogen gas jet [26, 27]. The measured laser energy was  $E \simeq 21$  J. Before the arrival of the LPA drive laser, an auxiliary pulse focused by an axicon lens was used to ionize and form a plasma channel by hydrodynamic expansion of an optical field-ionized plasma [36–38]. The

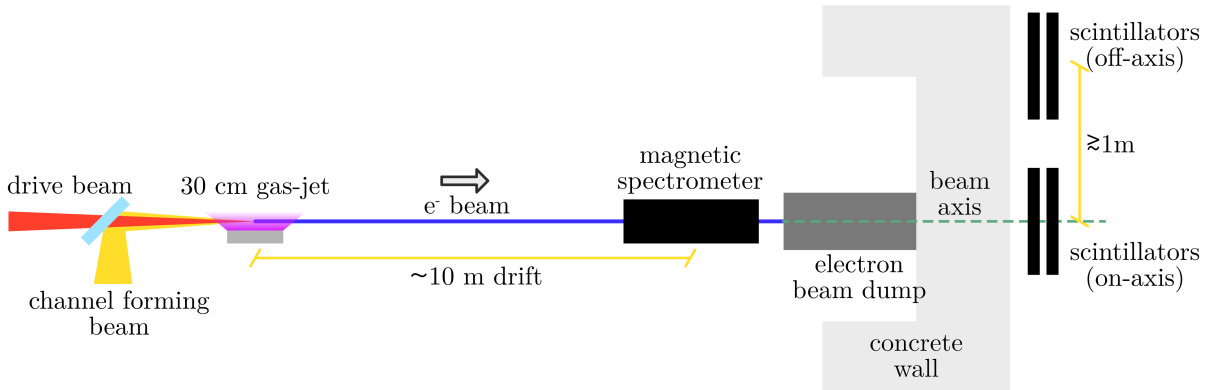


FIG. 3. Schematic of the experimental setup. The laser drive and channel-forming beams, on the left, are coupled into a 30 cm gas-jet, generating the electron beam. After a  $\sim 10$  m drift, the electron beam reaches the magnetic spectrometer and is then unloaded on the electron beam dump, where it produces the muons. The scintillators are placed behind the wall outside the experimental cave in two possible configurations. Each configuration includes a pair of scintillators close to each other (spaced a few cm), which were placed either along the beam axis, i.e., “on-axis” configuration, or  $\gtrsim 1$  m to the side of the beam axis, “off-axis” configuration. The scintillators are  $\simeq 10$  cm away from the back of the wall.

measured axial density was  $n_0 \approx 1 \times 10^{17} \text{cm}^{-3}$ . Ionization injection was triggered by a 1% nitrogen dopant extending over a region of the channel of length  $L_{\text{dop}}$ . For  $L_{\text{dop}} \approx 12$  cm, it was possible to achieve single, quasi-monoenergetic electron bunches with peak energy up to 9.2 GeV and charge extending beyond 10 GeV [27].

For this experiment,  $L_{\text{dop}} \approx 30$  cm, and the accelerator was run in a stable condition with electron beam spectrum shown in Fig. 4. The measured charge was in the range  $Q \simeq 45 - 250$  pC, integrated over energies above 2 GeV, and exponential-like energy spectra with tails extending to  $\sim 8$  GeV were observed.

These high-energy electrons are passed through a 1.08 T momentum analyzing dipole magnet (which bends the beams downward in the vertical direction) and then stopped in a dedicated electron beam dump, composed of 16 inches of lead, 37 inches of steel, and a final 72-inch block of concrete. After the electron beam dump, a 36 inches concrete wall separates the experimental cave from the measurement room. The length  $L$  of the electron beam dump, expressed in units of radiation lengths, is  $L \simeq 142$ , calculated using  $X_{0,\text{Pb}} = 0.56$  cm,  $X_{0,\text{Steel}} = 1.76$  cm, and  $X_{0,\text{Concrete}} = 11.6$  cm. The large thickness suppresses the propagation of secondary particles, such as photons, pions, kaons, electrons, and positrons. Muons only lose energy via ionization with a rate per unit density of about  $2 \text{MeVcm}^2/\text{g}$  [39]. Energy losses via Bremsstrahlung are negligible and are only relevant for muons with energies  $E \gtrsim 1$  TeV. This allows high energy muons to propagate through the beam dump and escape from its rear. From our simulations and from analytical estimates using the stopping power provided in Ref. [39], and considering the full beam dump and the cave wall, we obtain that a muon loses about  $E_L \simeq 4$  GeV

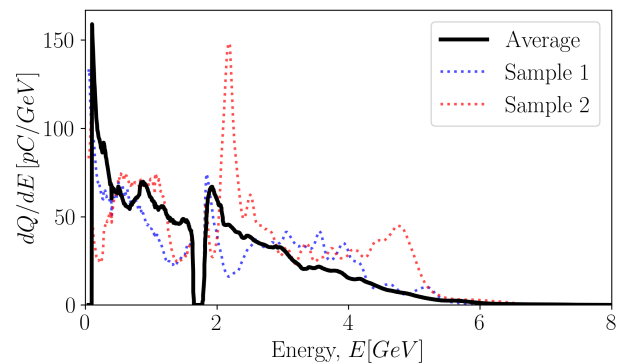


FIG. 4. The solid black line is the electron energy spectrum (averaged over 42 shots) used for muon generation experiments in December 2023. The beam is characterized by continuous, exponential-like spectrum with a tail extending to  $\sim 8$  GeV. Its integrated charge for energies  $E \geq 2$  GeV is  $Q \simeq 80$  pC. The blue and red dotted lines are two samples of single-shot electron spectra of the generated beams. The dip around 1.9 GeV is due to a physical gap in the magnetic spectrometer screens.

via ionization when reaching the other side of the wall. Ionization losses act as a filter for the low energy muons, as muons generated with energies  $E < E_L$  are absorbed during their propagation. Energy losses via ionization are energy-independent in the energy range of interest for our experiment, so the estimate holds for all the muons produced in the interaction. These losses must be taken into account when designing a muon source as they typically define the muon penetration range into the imaged sample. Muons propagating in the material are subject

to scattering, which increases the final muon beam divergence. An estimate of the final angle accumulated by a muon of momentum  $p$ , that is with normalized velocity  $\beta = v/c = p/(m_\mu c\gamma)$ , via multiple scattering after propagating a distance  $d$  in a material with radiation length  $X_0$  can be obtained using the approximate formula [40]

$$\sigma_\theta^2 = \left( \frac{13.6 \text{ MeV}}{p\beta} \right)^2 \frac{d}{X_0} \left[ 1 + 0.038 \log \left( \frac{d}{\beta^2 X_0} \right) \right]^2, \quad (1)$$

derived from Moliere's scattering theory [41]. Eq. (1) neglects energy losses during the propagation, but we can apply it using the average energy of a muon to roughly estimate the final angular aperture of the beam. For instance, for muons with an initial energy  $E_0 = 4 \text{ GeV}$  the final rms divergence is on the order of  $\sigma_\theta \simeq 100 \text{ mrad}$ . Given a total propagation length from the creation point, i.e., the beam dump and the wall, of about  $L \simeq 4 \text{ m}$ , the expected beam rms size behind the wall is  $\sigma_r \simeq 50 \text{ cm}$ .

### A. Detectors

A scintillator-based radiation detector is employed for beam pulse monitoring and muon identification behind the beam dump. The setup consists of two panels of scintillating plastic (1 cm thick Polystyrene, total area of  $500 \text{ cm}^2/\text{panel}$ ) each optically coupled to a photomultiplier tube (PMT). Each PMT signal is fed into a shaping amplifier and, along with a logic trigger indicating the laser pulse timing, read out by a 50 MHz Analog-to-Digital Converter (ADC). A NIM logic unit giving the 'AND' of both channel discriminators initiates a  $50 \mu\text{s}$  readout window of the ADC, which is saved for offline analysis. The time resolution of particle interaction in the scintillator is limited by the period between samples of the ADC, which is 20 ns.

Fig. 3 shows the experimental apparatus behind the beam dump. The scintillator panels are arranged in two different orientations used to monitor the muon production at different angles from the beam direction. We identify in particular an "on-axis" configuration, where the scintillator is placed along the beam path, and an "off-axis" configuration, with the scintillator moved  $\gtrsim 1 \text{ m}$  off the beam axis.

Muons in the 1-10 GeV energy range are minimum ionizing particles, however, below this range, their energy loss per unit distance rises sharply [39]. Muons (antimuons) of sufficiently low energy, on the order of 20 MeV, can be stopped by the layers of plastic scintillator, and their decay to an electron (positron) and two neutrinos within the plastic can subsequently be observed with a lifetime  $\tau_\mu = 2.2 \mu\text{s}$ . Stopped muon decays are identified in the experimental apparatus via the ionization from the daughter electron, which manifests as a second light pulse following the initial trigger. By studying the decay time distribution, a positive muon identification can be made by checking consistency with the well-known muon lifetime.

## IV. EXPERIMENTAL RESULTS

During the experiment, we operated the laser at a frequency of 0.1 Hz. The radiation generated by the accelerated electron beam unloaded on the electron beam dump served as a trigger to activate the scintillators. Of the muons produced in the interaction, some reach the detectors with an energy range  $0 \leq E \lesssim 20 \text{ MeV}$ . These muons stop in the Polystyrene until they decay, generating a delayed signal. We assigned the time  $t = 0$  to each trigger

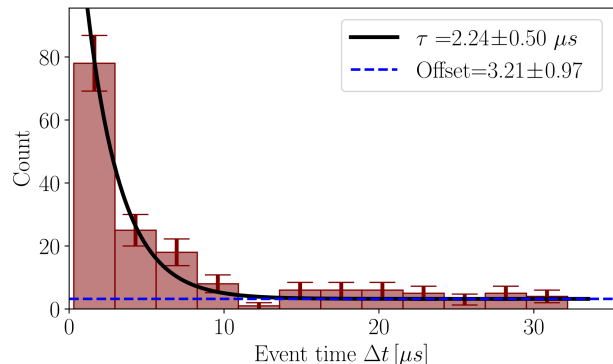


FIG. 5. Count of time delay from the initial trigger,  $t = 0$ . Error bars are obtained under a Poisson distribution. By fitting with the exponential function  $f(t) = A \exp(-t/\tau) + C$ , that is assuming signal from muon decay (black solid line) and a constant background (blue dashed line), we obtain  $\tau = 2.24 \pm 0.50 \mu\text{s}$  and  $C = 3.21 \pm 0.97$ .

and collected the subsequent signals into the histogram shown in Fig. 5. The dataset refers to a roughly two hour period, i.e., 760 shots, in which we measured electron beams with the average spectrum shown in Fig. 4, i.e., with  $Q = 80 \text{ pC}$  for  $E > 2 \text{ GeV}$ . By fitting the histogram with the exponential function  $f(t) = A \exp(-t/\tau) + C$ , we obtain the lifetime  $\tau = 2.24 \pm 0.50 \mu\text{s}$  and a constant background  $C = 3.21 \pm 0.97$ . The measurement of the decay time is compatible with the decay of stopped muons, i.e.,  $\tau_\mu = 2.2 \mu\text{s}$ . Given that the total number of muon candidates recorded is  $N_{tot} = 165$ , and that we used 12 bins for the histogram, the number of detected muons is  $N_\mu = 126 \pm 12$ , while the number of background events is  $N_b = 39 \pm 12$ . We deem the contribution of cosmic muons negligible because the average flux of muons from cosmic rays from all angles at sea level is about  $F \simeq 147 \text{ m}^{-2}\text{s}^{-1}$  [5], i.e., the expected number of muons hitting the scintillator surface  $\Sigma \simeq 0.05 \text{ m}^2$  within a  $\Delta t = 35 \mu\text{s}$  interval after a laser shot is  $\simeq 3 \times 10^{-4}$ . The flat background is produced by the incoming electron beam, as scintillators with the beam off only show signals compatible with cosmic muons. In particular, we identified the cause of the background as being generated by the photons emitted in the neutron capturing in the shielding. After the initial burst of radiation generated by the incoming electron beam, charac-

	$\tau$ [ $\mu\text{s}$ ]	$C$
Total	$2.24 \pm 0.50$	$3.21 \pm 0.97$
Off-axis	$2.39 \pm 0.54$	$2.70 \pm 0.89$
On-axis	$1.74 \pm 0.66$	$0.58 \pm 0.32$

TABLE I. Lifetime  $\tau$  and background  $C$  resulting from fitting the histogram of the total, off-axis, and on-axis event, respectively.

terized by a Bremsstrahlung spectrum very localized in time, i.e.,  $\Delta t \lesssim 1$  ns, slower particles, such as neutrons, travel through the experimental cave and reach the back wall on the  $\mu\text{s}$  to ms time scales. When neutrons are stopped in the shielding concrete, they generate photons with frequencies related to characteristic levels of atomic excitation [42] of, for instance, Silicon and Oxygen, the elements that account for the highest fraction of the concrete mass. The produced MeV photons hit the scintillators, scattering on its electrons and generating a signal in the PMTs. The presence of such neutrons is confirmed by the neutron monitors inside and outside the cave.

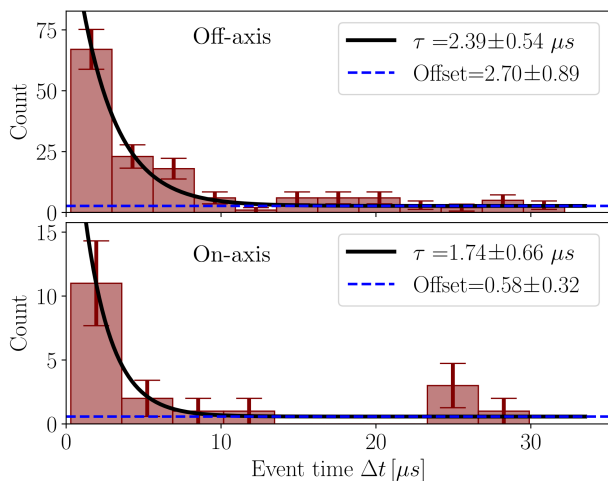


FIG. 6. Count of time delay from the initial trigger,  $t = 0$ , separated for scintillators on the beam propagation axis (bottom panel) and moved to the side (top panel). Error bars are obtained under a Poisson distribution. The exponential fits result in  $\tau = 2.39 \pm 0.54 \mu\text{s}$  and  $C = 2.70 \pm 0.89$ , and  $\tau = 1.74 \pm 0.66 \mu\text{s}$  and  $C = 0.58 \pm 0.32$  for the off-axis and on-axis case respectively.

In Fig. 6 we separate the muon counting in on-axis and off-axis measurements. These correspond to muon decay times measured with the scintillators placed on the beam axis and  $\sim 1$  m to its side, respectively. The top and bottom panels show the muon counting registered from an off-axis and on-axis scintillator, respectively. Each of the two measurements was performed in a 1-hour time interval, and the off-axis configuration measures more muons than the on-axis one. In particular, by repeating the analysis on the off-axis and on-axis counting histograms,

we obtain  $\tau = 2.39 \pm 0.54 \mu\text{s}$  and  $C = 2.70 \pm 0.89$  and  $\tau = 1.74 \pm 0.66 \mu\text{s}$  and  $C = 0.58 \pm 0.32$ , respectively, from which we estimate the number of stopped muons as  $N_{\mu}^{\text{off}} = 114 \pm 11$  and  $N_{\mu}^{\text{on}} = 14 \pm 3$ . We obtain the off-axis and on-axis probabilities of a muon detection per shot per scintillator as  $P^{\text{off}} = (14.4 \pm 1.4) \%$  and  $P^{\text{on}} = (1.9 \pm 0.5) \%$  respectively, where we used the number of shots  $N_{\text{shots}}^{\text{off}} = 386$  and  $N_{\text{shots}}^{\text{on}} = 374$ . As we will see in the next section, such a large muon count away from the beam propagation axis can be explained by taking into account the contribution of muons generated in the decay of mesons.

We have shown in this section that the analysis of the scintillator signals revealed unambiguous detection of muons generated by the electron beams. In the next section, we will show that computational modeling of the experiment reproduces the measurements and identifies the source the muon count far from the beam axis.

## V. SIMULATION RESULTS

We performed numerical simulations of the muon production using a custom code based on the Geant4 toolkit. Our code implements an accurate model of the beam dump and of the wall between the beam dump and the measurement room. In addition, we included two of the high- $Z$  laser diagnostics, a wedge and power meter, as well as the magnetic spectrometer since they are placed along the beam path, even though they do not interact with well-aligned electron beams. The magnetic spectrometer, although physically implemented in the code, was turned off in the simulations. We implemented a *sensitive detector*, a detector in Geant4 that is a virtual screen behind the wall to record the passage of every particle. For each particle hitting the detector, its information, e.g., phase space, detection time, and generating process, are saved. Moreover, we implemented copies of the scintillators in order to model their response within the same simulation framework, that is therefore fully self-consistent. More details on the code can be found in the appendix. We initialized the electron beam according to its average spectral profile, shown in Fig. 4, limited to energies  $E > 2$  GeV, i.e., with a total charge  $Q = 80$  pC, and with a *rms* divergence  $\sigma_{\theta} \simeq 0.1$  mrad that we chose in order to simplify the simulations using a quasi-pencil beam. Fig. 7 shows the simulation setup, including, from right to left, following the beam path, the two laser diagnostics, the magnetic spectrometer, the electron beam dump, and the large wall behind the electron beam dump. The width and height of the wall coincide with the Geant4 *world*, i.e., the maximum geometry extent, therefore it is not possible for a particle to travel around the wall and reach the detectors, not shown in the figure, behind the wall itself. In Fig. 7, red trajectories are the electrons, including the primary ones coming from the direction of the arrow, while blue trajectories represent the positrons. The cyan and yellow

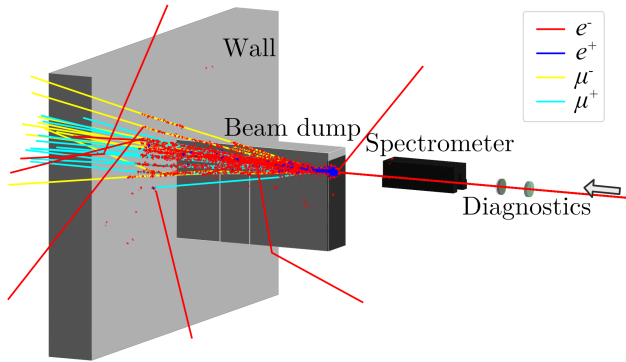


FIG. 7. Scheme of the simulation setup implemented in Geant4 to model the experiment. From right to left, the arrow shows the beam direction. The two disks are laser diagnostics with some high- $Z$  layers. The black box is the magnetic spectrometer and, following, there is the beam dump. On the left, the concrete wall that separates the experimental cave from the measurement room, where the scintillators are placed. The red lines are electron trajectories, the blue ones positrons. Positive and negative muons are respectively cyan and yellow. We filtered neutrons and photons for the sake of visualization.

trajectories are, respectively,  $\mu^+$  and  $\mu^-$ , which are created in the early lead region of the dump and propagate through it, reaching the measurement room. For the sake of visualization, we removed photon and neutron trajectories from the picture. As explained in Sec. II, we expect the majority of high energy photons to be produced in the beam direction via Bremsstrahlung. Neutrons are produced in the high- $Z$  layers of the beam dump and emitted isotropically in space. Electrons with energies ranging from keV to MeV are extracted via ionization by the muon passage and, in the majority of cases, quickly reabsorbed. Electrons extracted close to the back of the wall can have enough energy to escape and propagate in the measurement room. Such electrons are represented in Fig. 7 by the red trajectories that generate from the muons ones.

We show in the top panel of Fig. 8 the simulated energy spectrum of muons sampled at  $5X_0$  inside the electron beam dump, i.e.,  $\simeq 3$  cm inside the lead block (black line) and on the detector in the measurement room (blue line). As we mentioned earlier, muons predominantly lose energy via ionization when propagating through dense materials. Due to the electron beam dump and wall this results in  $E_L \simeq 4$  GeV muon energy loss before the detection point. To verify the simulation result, we estimated the energy losses by integrating the equation of motion of a muon moving in a straight trajectory through the shielding configuration, using the stopping power tabulated in Ref. [39]. Assuming an initial 8 GeV energy, we show the muon energy in function of its propagation through the dump in the bottom panel of Fig. 8. As we mentioned previously, in a broad energy range

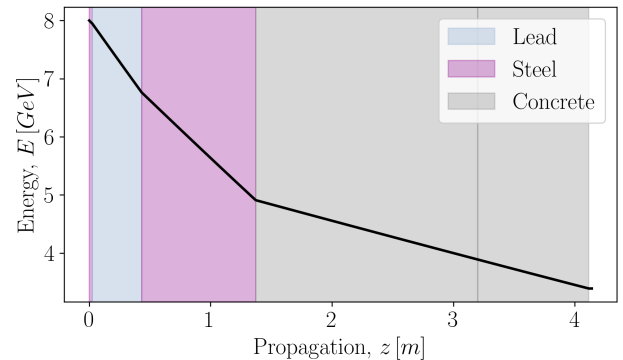
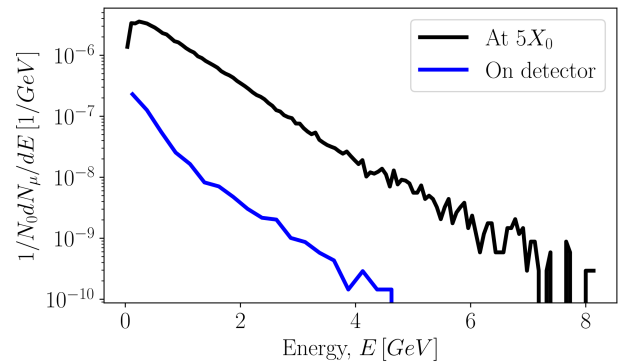


FIG. 8. Top panel: muon energy spectra obtained via Geant4 simulations of a perfectly aligned electron beam with energy shown in Fig. 4. The black line is the energy spectrum sampled 5 radiation lengths into the dump. The blue line is the spectrum on the virtual screen behind the external wall. The difference in the spectra is due to the ionization losses. Both spectra are normalized per primary electron. Bottom panel: muon energy in function of its propagation in the dump and external wall, assuming an initial  $E_0 = 8$  GeV. The result is obtained by integrating the equation of motion, assuming a straight trajectory, using the stopping power provided in Ref. [39].

$1 \text{ GeV} \leq E \leq 10 \text{ GeV}$  the stopping power is substantially energy-independent, thus the calculation applies to all the generated muons. This agrees with the simulated results as we note that we obtain the muon spectrum at the detection point by shifting the one sampled inside the converter, i.e., the electron beam dump, towards lower energies.

Figure 9 shows the expected flux of muons obtained from an 80 pC electron beam with the initial energy spectrum shown in Fig. 4. The beam size on the virtual detector is  $\sigma_x \simeq \sigma_y \simeq 40$  cm. Fig. 9 shows a negligible flux of muons outside a cone of narrow aperture  $\sigma_\theta \simeq 100$  mrad, which agrees with the expectation of muons generated via Bethe-Heitler. In order to explain the detection of muons away from the beam axis, we need to take into account the pointing fluctuations of the electron beam, characterized during the experiment with  $\sigma_\theta \simeq 3$  mrad. Despite this value is negligible compared to the aper-

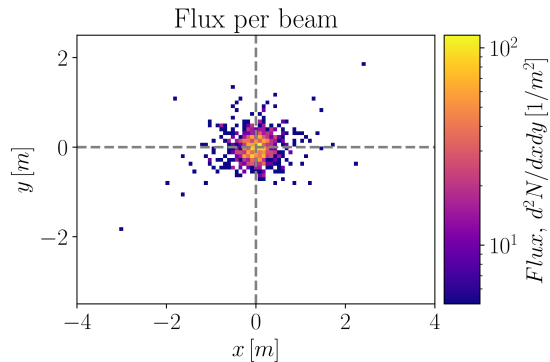


FIG. 9. Muon flux behind the external wall computed using Geant4 for a perfectly aligned beam. The calculation assumes an initial  $Q = 80$  pC electron beam perfectly aligned on the beam axis, i.e., it does not interact with the laser diagnostics and the magnetic spectrometer. The muon flux on the beam axis is  $F \simeq 2 \times 10^2 \text{ m}^{-2}$ . An inspection of the muons shows that all of them are generated via Bethe-Heitler. The dashed grey lines represent the beam center.

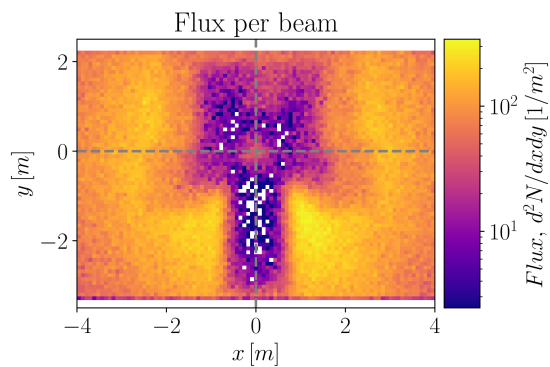


FIG. 10. Muon flux behind the external wall computed using Geant4 for a misaligned electron beam. The calculation assumes an initial  $Q = 80$  pC electron beam, with an initial misalignment  $\theta = 1.5$  mrad. The shift is sufficient for the electron beam to interact with the laser diagnostics and the magnetic spectrometer. The central disk of muons generated via Bethe-Heitler is essentially unaffected, showing a flux on the beam axis  $F \simeq 2.5 \times 10^2 \text{ m}^{-2}$ , but muons generated in meson decay contribute to a quasi-isotropic flux all around the chamber. The dashed grey lines represent the beam center.

ture of the emission cone, it is enough for the electron beam to interact with the laser diagnostics placed before the magnetic spectrometer, which have an angular acceptance of 1.2 mrad, and with the magnetic spectrometer itself. Since all these elements are made of high- $Z$  materials, i.e., aluminum, fused silica, and steel, a beam passing through them produces muons via Bethe-Heitler process and mesons from photoproduction, as illustrated in Sec. II. Mesons do not encounter the same amount of ma-

terial as when they are produced deep inside the electron beam dump and therefore they are not reabsorbed, propagating in the experimental cave. Once these mesons decay, the low energy muons that are produced do not need to traverse the electron beam dump and have enough energy to propagate into the external wall and be detected by the scintillators. This is demonstrated in Fig. 10, where we show the simulated flux of muons per beam, assuming an initial beam beam deviation of 1.5 mrad from the axis. It is interesting to note that the central disk of muons, generated via Bethe-Heitler, is almost unaffected by the misalignment, while the muons generated via meson decay, quasi-isotropically distributed, contribute significantly to the final flux of muons far from the beam axis. The central shade in the picture resembles the shade of the magnetic spectrometer and the beam dump, which demonstrates that mesons are produced and decay into muons before the spectrometer, resulting in a radiography of the two elements onto the virtual detector. The lack of the filtering power provided by the electron beam dump also explains the higher background noise recorded in off-axis measurements. Photons generated in the interaction and in the neutron capturing inside the shielding, can traverse the wall away from the beam dump, scattering on the electrons of the scintillators and triggering signal.

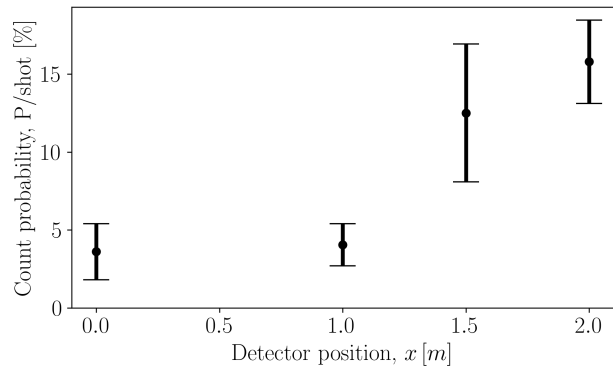


FIG. 11. Simulated probability of counting a muon in a scintillator per incoming LPA beam in function of the horizontal position of the scintillator. Results are obtained using a model of the scintillator implemented in Geant4 and assuming a misaligned electron beam. The probabilities at  $x = 0$  and  $x \gtrsim 1.5$  m agree well with the values measured in the experiment.

The scintillator models implemented in the code allow us to directly count the muons that stop and decay into them, reconstructing the signal we obtained in the experiment. We can see in Fig. 11 the simulated probability of counting a muon per LPA beam in a detector placed at the beam height as a function of the detector horizontal position. The results agree quite well with the measurements. We computed a probability of a muon stopping in a scintillator  $P = (12.5 \pm 4.4)\%$  for a scintillator placed

1.5 m to the side of the beam axis and  $P = (3.6 \pm 1.8)\%$  for a scintillator sitting on the beam axis. As it was shown in Sec. IV, the measured values for those probabilities are  $P^{\text{off}} = (14.4 \pm 1.4)\%$  and  $P^{\text{on}} = (1.9 \pm 0.5)\%$  respectively. Although it was not possible to match the horizontal position of the detector in the simulation, the result demonstrates that the muon count matches the one of a detector placed outside of the shadow of the magnetic spectrometer, i.e., the detector simulated at  $x \gtrsim 1.5$  m, where the flux of muons is roughly uniform. Matching both the ratio and the absolute numbers of the muon count on and off the beam axis confirms the reliability of the simulation tools that we developed and that can be therefore used to design future experiments.

The simulation results show remarkable agreement with the experimental measurements. However, our simulations include a few assumptions. First, we only presented simulations performed with an inactive spectrometer. Despite verifying that the resulting physical picture is unchanged except for the expected downward vertical shift of the generated beam induced by the magnet, the computational cost of Geant4 simulations with a magnetic field is large, thus accumulating reasonable statistics is challenging, because a lower number of events can be tested. Without the magnetic spectrometer, we needed consider the different horizontal positions between the simulated and the actual detector far from the axis. In fact, including the vertical bending induced by the magnetic field,  $\Delta y \gtrsim -50$  cm, a detector placed at the beam height and  $\gtrsim 1$  m to its side falls outside the shadow of the magnetic spectrometer. Simulating the behavior of a scintillator at  $x \gtrsim 1.5$  m accounts for this difference and yields the correct result for the muon count.

Second, we assumed an almost-pencil beam, i.e., very low divergence, and reproduced the effects of its misalignment by changing the direction of the propagation axis. This approach provides a simple description, without affecting the final conclusions, as one could see a highly divergent beam as a combination of aligned and a misaligned sub-beams. In fact, all the physics we have discussed in this work is linear with the initial beam charge and effects can be superimposed.

The present work shows that LPA generated electron beams possess an outstanding capability of generating directional muon beams. In fact, the performance of the source can be improved by orders of magnitude by increasing the initial electron energy due to a conjunction of multiple effects. The properties of the Bremsstrahlung cascade are such that the yield of particles from pair production for an optimized target scales roughly linearly with the initial beam energy [30], although the scaling could be either sub- or super-linear depending on the target geometry and the exact energy range [17]. Moreover, higher initial energies result in a more collimated muon beam, i.e., higher flux, and a higher maximum muon energy. Muons from meson decay, on the other hand, do not present the same favorable scaling with energy, as a crucial parameter for their decay is the distance from the

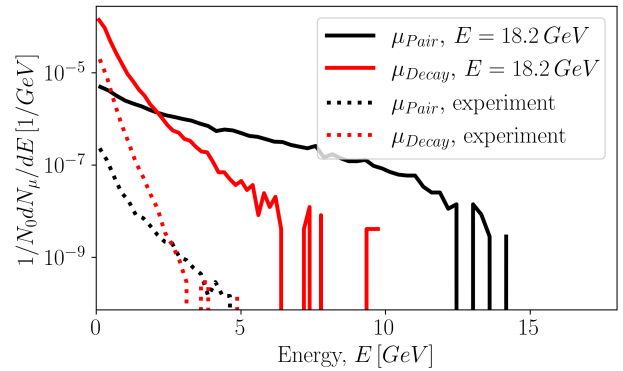


FIG. 12. Spectra of muons behind the wall, obtained using Geant4, integrated over the whole surface and differentiated by the muon generating process. The black lines show the spectrum of pair-produced muons, the red lines muons generated via meson decay. The solid lines refer to a monochromatic, 18.2 GeV, 26 pC electron beam obtained in simulations of staging LPAs using two 19 J laser pulses, with BELLA laser parameters. The dotted lines refer to the spectra obtained using the experimental electron beam with spectrum as in Fig. 4. Increasing the electron beam energy improves the source quality by producing a higher yield of directional and high energy muons.

converter target. We compared simulations of the muons produced by the experimental electron beam to the ones produced by a higher energy beam achievable, for instance, by staging two LPA sections each powered by a 19 J BELLA-like laser pulse (which is not unrealistic for the current 40 J facility). Fig. 12 shows the simulated muon spectra, integrated over the entire wall surface, resulting from the interaction of the average 80 pC beam obtained in our experiment and of a 26 pC monochromatic beam with  $E = 18.2$  GeV, produced in simulations of staging acceleration using two LPA sections, impinging on the shielding configuration, respectively. The spectra are normalized per initial electron. The plot demonstrates that by increasing the source energy, the overall quality of the muon source improves. Muons from meson decay still form the majority of the produced muons at low energy, however their cutoff energy is only marginally increased. On the other hand, muons produced via pair production extend to higher energies and, even accounting for the energy losses induced by the shielding, they possess the strong penetrating power required for imaging applications.

These results motivate us to design future experiments and applications based on  $E > 10$  GeV electron beams. While for the present work we relied on the electron-to-muon conversion offered by the shielding, it is possible to design optimized converter targets, as shown in Fig. 2, where the muon flux can be maximized and the energy losses minimized. The optimal energy of the electron beam is determined by the imaging sample considered, due to the mentioned effect of ionization losses. With

the Geant4-based simulation tool that we developed, we can investigate the properties of the resulting beam and design an appropriate detection scheme to pick up signals from the high-energy muons before and after an imaging object. It is also possible to equip our code with imaging reconstruction algorithms that enable start-to-end simulations, i.e., from the electron beam to the final imaging result, which would let us tailor the design of a converter target and the required shielding.

## VI. CONCLUSIONS

In this paper, we presented the implementation of a high-energy and directional muon source based on laser-plasma accelerated electron beams obtained using the BELLA PW laser. The electron beams were generated via ionization injection of an unlocalized dopant and accelerated using a 21 J laser pulse, which yielded beams with broad energy spectra reaching up to 8 GeV, low divergence, and pointing fluctuations of 3 mrad [27]. When such beams impinged on the electron beam dump or grazed other high- $Z$  elements along their path, muons were generated via pair production and meson decay. We identified  $N = 126 \pm 12$  muon detections during two hours operation, sampled from the low energy part of the generated beam, and we characterized the resulting muon flux via simulations and experiments, noting that the two production mechanisms could be spatially distinguished. Muons from pair production are characterized by a high-energy, up to the energy of the initial electrons, a low-divergence, and a strong directionality along the incoming beam path. These characteristics make them very suitable for imaging applications as the illumination of a target can be optimized to maximize their flux and their tracking in and out from the target itself. The energy and number of pair produced muons scales with the initial electron beam energy and charge and can be tuned to fit the application requirements.

Muons from decay of mesons make up the majority of muons near the converter. They are characterized by a quasi-isotropic angular distribution and by a sharp cut-off at high energies, therefore their contribution to the muon flux in the forward direction is very weak. Moreover, their energy does not scale with the initial electron energy and, therefore, they do not offer a strong penetrating power. It is not desirable to rely on them in applications that require high fluxes at a distance. In our experiment and simulations we showed that muons generated via meson decay can be detected away from the beam path, where they are not filtered by the electron beam dump.

LPA accelerated electron beams possess outstanding properties to generate muon fluxes orders of magnitude higher than what is naturally available with cosmic rays. In particular, while the flux of cosmic muons through an horizontal imaging setup with an aperture  $\theta = 100$  mrad is  $F \simeq 0.1 \text{ m}^{-2}\text{s}^{-1}$ , LPA beams with

energies and charges in the range, respectively,  $E \sim (1 - 10) \text{ GeV}$  and  $Q \sim (10 - 500) \text{ pC}$  and operated at repetition rates of  $(0.1 - 1) \text{ Hz}$  provide muon fluxes up to  $F \simeq 10^2 - 10^4 \text{ m}^{-2}\text{s}^{-1}$ . Near future LPA and laser technology developments, e.g., staged acceleration and pulse delivery at the kHz repetition rate, can boost this property by orders of magnitude. Using the same simulation tools we used to understand the experimental results, we can design future muography application based on high-energy electron beams and detectors suitable for muon scattering image reconstruction.

This experiment proves the feasibility of a muon source based on LPA-generated electron beams. It is an important result to establish the readiness of the LPA technology for applications and to motivate the development of high repetition rate laser systems, which could push applications like muography to unprecedented capabilities, offering muon fluxes orders of magnitude higher than cosmic rays.

## ACKNOWLEDGMENTS

The authors would like to thank Adam Davis, Brian Dorney, Francesca Kukral, Hans Malik, and Scott Wolin of Northrop Grumman Corporation, Ryan Heller of the Lawrence Berkeley National Laboratory for the insightful discussions, and Zachary Eisentraut, Mark Kirkpatrick, Federico Mazzini, Nathan Ybarrolaza, Derrick McGrew, Paul Centeno, Teo Maldonado Mancuso, Art Magana, Joe Riley, Mackinley Kath, and Chetanya Jain of the Lawrence Berkeley National Laboratory for technical support on experiments. D.T. is grateful to Sarah Schröder and Stepan Bulanov for the enlightening conversations. This work was supported by the Defence Advanced Research Projects Agency (DARPA), the Director, Office of Science, Office of High Energy Physics, of the U.S. Department of Energy under Contract No. DE-AC02-05CH11231, and used the computational facilities at the National Energy Research Scientific Computing Center (NERSC).

### Appendix: Modeling the experiments with a Geant4-based code

We performed simulations of the experimental campaign with a custom application developed using Geant4. The code defines the geometry of the experimental chamber as closely as possible, as we retained shapes and materials of each of the elements. The implementation includes two laser diagnostics, a wedge and a power meter, the magnetic spectrometer, the beam dump with all its internal layers and the external wall. The electron beam can be initialized freely using macros, and its energy spectrum, initial position and direction and its divergence can be chosen arbitrarily. The code uses the predefined `QGSP_BERT_EMZ` physics package. It in-

cludes a high precision model for neutron propagation, that we used to understand background noise, and for the electromagnetic interaction. The code accounts for the muon pair production process, which has to be manually added. During our time using and benchmarking the code we updated several Geant4 versions, but the results presented in this paper are obtained with Geant4 v11.2. While the version v11.0 returns consistent values, we noticed during our investigation that version v11.1 does not yield the same results for muon production. The issue was addressed in subsequent releases (see Geant4 v11.2 Release Notes).

The code is equipped with several diagnostics, including sensitive detectors in the dump that track the development of the Bremsstrahlung cascade, a sensitive detector behind the wall that captures all the particles leaving the chamber and a model of the scintillators. We save the phase space and some relevant information about particles that cross them that generate most of the plots shown in the paper. The scintillators are constructed using the same material and size as the real detectors and they are programmed to return particles that stop within their boundaries, from which we can extract the number of muons detected.

- 
- [1] D. Schulte, *The Muon Collider* (JACOW Publishing, Geneva, Switzerland, 2022) pp. 821–826, iSSN: 2673-5490.
- [2] A. Keshavarzi, K. S. Khaw, and T. Yoshioka, Muon g-2: A review, *Nuclear Physics B* **975**, 115675 (2022).
- [3] M. S. Zisman, Proton beam requirements for a neutrino factory and muon collider, in *Applications of High Intensity Proton Accelerators* (WORLD SCIENTIFIC, 2010) pp. 145–150.
- [4] S. Bouteille, D. Attié, P. Baron, D. Calvet, P. Magnier, I. Mandjavidze, S. Procureur, M. Riallot, and M. Winkler, A Micromegas-based telescope for muon tomography: The WatTo experiment, *Nuclear Instruments and Methods in Physics Research Section A: Accelerators, Spectrometers, Detectors and Associated Equipment* **834**, 223 (2016).
- [5] Particle Data Group, R. L. Workman, V. D. Burkert, V. Crede, E. Klempt, U. Thoma, L. Tiator, K. Agashe, G. Aielli, B. C. Allanach, C. Amsler, M. Antonelli, E. C. Aschenauer, D. M. Asner, H. Baer, S. Banerjee, R. M. Barnett, L. Baudis, C. W. Bauer, J. J. Beatty, V. I. Belousov, J. Beringer, A. Bettini, O. Biebel, K. M. Black, E. Blucher, R. Bonventre, V. V. Bryzgalov, O. Buchmuller, M. A. Bychkov, R. N. Cahn, M. Carena, A. Cecucci, A. Cerri, R. S. Chivukula, G. Cowan, K. Cranmer, O. Cremonesi, G. D’Ambrosio, T. Damour, D. de Florian, A. de Gouvêa, T. DeGrand, P. de Jong, S. Demers, B. A. Dobrescu, M. D’Onofrio, M. Doser, H. K. Dreiner, P. Eerola, U. Egede, S. Eidelman, A. X. El-Khadra, J. Ellis, S. C. Eno, J. Erler, V. V. Ezhela, W. Fetscher, B. D. Fields, A. Freitas, H. Gallagher, Y. Gershtein, T. Gherghetta, M. C. Gonzalez-Garcia, M. Goodman, C. Grab, A. V. Gritsan, C. Grojean, D. E. Groom, M. Grünewald, A. Gurtu, T. Gutsche, H. E. Haber, M. Hamel, C. Hanhart, S. Hashimoto, Y. Hayato, A. Hebecker, S. Heinemeyer, J. J. Hernández-Rey, K. Hikasa, J. Hisano, A. Höcker, J. Holder, L. Hsu, J. Huston, T. Hyodo, A. Ianni, M. Kado, M. Karliner, U. F. Katz, M. Kenzie, V. A. Khoze, S. R. Klein, F. Krauss, M. Kreps, P. Krizan, B. Krusche, Y. Kwon, O. Lahav, J. Laiho, L. P. Lellouch, J. Lesgourgues, A. R. Liddle, Z. Ligeti, C.-J. Lin, C. Lippmann, T. M. Liss, L. Littenberg, C. Lourenço, K. S. Lugovsky, S. B. Lugovsky, A. Lusiani, Y. Makida, F. Maltoni, T. Mannel, A. V. Manohar, W. J. Marciano, A. Masoni, J. Matthews, U.-G. Meißner, I.-A. Melzer-Pellmann, M. Mikhasenko, D. J. Miller, D. Milstead, R. E. Mitchell, K. Mönig, P. Molaro, F. Moortgat, M. Moskovic, K. Nakamura, M. Narain, P. Nason, S. Navas, A. Nelles, M. Neubert, P. Nevski, Y. Nir, K. A. Olive, C. Patrignani, J. A. Peacock, V. A. Petrov, E. Pianori, A. Pich, A. Piepke, F. Pietropaolo, A. Pomarol, S. Pordes, S. Profumo, A. Quadt, K. Rabbertz, J. Rademacker, G. Raffelt, M. Ramsey-Musolf, B. N. Ratcliff, P. Richardson, A. Ringwald, D. J. Robinson, S. Roesler, S. Rolli, A. Romaniouk, L. J. Rosenberg, J. L. Rosner, G. Rybka, M. G. Ryskin, R. A. Ryutin, Y. Sakai, S. Sarkar, F. Sauli, O. Schneider, S. Schönert, K. Scholberg, A. J. Schwartz, J. Schwiening, D. Scott, F. Sefkow, U. Seljak, V. Sharma, S. R. Sharpe, V. Shiltsev, G. Signorelli, M. Silari, F. Simon, T. Sjöstrand, P. Skands, T. Skwarnicki, G. F. Smoot, A. Soffer, M. S. Sozzi, S. Spanier, C. Spiering, A. Stahl, S. L. Stone, Y. Sumino, M. J. Syphers, F. Takahashi, M. Tanabashi, J. Tanaka, M. Taševský, K. Terao, K. Terashi, J. Terning, R. S. Thorne, M. Titov, N. P. Tkachenko, D. R. Tovey, K. Trabelsi, P. Urquijo, G. Valencia, R. Van de Water, N. Varelas, G. Venanzoni, L. Verde, I. Vivarelli, P. Vogel, W. Vogelsang, V. Vorobyev, S. P. Wakely, W. Walkowiak, C. W. Walter, D. Wands, D. H. Weinberg, E. J. Weinberg, N. Wermes, M. White, L. R. Wiencke, S. Willocq, C. G. Wohl, C. L. Woody, W.-M. Yao, M. Yokoyama, R. Yoshida, G. Zanderighi, G. P. Zeller, O. V. Zenin, R.-Y. Zhu, S.-L. Zhu, F. Zimmermann, and P. A. Zyla, Review of Particle Physics, *Progress of Theoretical and Experimental Physics* **2022**, 083C01 (2022).
- [6] K. Morishima, M. Kuno, A. Nishio, N. Kitagawa, Y. Manabe, M. Moto, F. Takasaki, H. Fujii, K. Satoh, H. Kodama, K. Hayashi, S. Odaka, S. Procureur, D. Attié, S. Bouteille, D. Calvet, C. Filosa, P. Magnier, I. Mandjavidze, M. Riallot, B. Marini, P. Gable, Y. Date, M. Sugiura, Y. Elshayeb, T. Elnady, M. Ezzy, E. Guerriero, V. Steiger, N. Serikoff, J.-B. Mouret, B. Charlès, H. Helal, and M. Tayoubi, Discovery of a big void in Khufu’s Pyramid by observation of cosmic-ray muons, *Nature* **552**, 386 (2017), publisher: Nature Publishing Group.
- [7] A. Nishio, K. Morishima, K. Kuwabara, and M. Nakamura, Development of Nuclear Emulsion Detector for Muon Radiography, *Physics Procedia 26th International Conference on Nuclear Tracks in Solids (ICNTS26) Kobe, Japan 15th – 19th September 2014*, **80**, 74 (2015).
- [8] H. Tanaka, K. Nagamine, N. Kawamura, S. N. Naka-

- mura, K. Ishida, and K. Shimomura, Development of a two-fold segmented detection system for near horizontally cosmic-ray muons to probe the internal structure of a volcano, *Nuclear Instruments and Methods in Physics Research Section A: Accelerators, Spectrometers, Detectors and Associated Equipment* **507**, 657 (2003).
- [9] X. Hu, L. S. Ökvist, E. Åström, F. Forsberg, P. Checchia, G. Bonomi, I. Calliari, P. Calvini, A. Donzella, E. Faraci, F. Gonella, J. Klinger, D. Pagano, A. Rigoni, P. Zanuttigh, P. Ronchese, M. Urbani, S. Vanini, A. Zenoni, and G. Zumerle, Exploring the Capability of Muon Scattering Tomography for Imaging the Components in the Blast Furnace, *ISIJ International* **58**, 35 (2018).
- [10] H. Fujii, K. Hara, S. Hashimoto, F. Ito, H. Kakuno, S. Kim, M. Kochiyama, K. Nagamine, A. Suzuki, Y. Takada, Y. Takahashi, F. Takasaki, and S. Yamashita, Performance of a remotely located muon radiography system to identify the inner structure of a nuclear plant, *Progress of Theoretical and Experimental Physics* **2013**, 073C01 (2013).
- [11] H. Fujii, K. Hara, K. Hayashi, H. Kakuno, H. Kodama, K. Nagamine, K. Sato, K. Sato, S.-H. Kim, A. Suzuki, K. Takahashi, and F. Takasaki, Detection of on-surface objects with an underground radiography detector system using cosmic-ray muons, *Progress of Theoretical and Experimental Physics* **2017**, 053C01 (2017).
- [12] G. Jonkmans, V. N. P. Anghel, C. Jewett, and M. Thompson, Nuclear waste imaging and spent fuel verification by muon tomography, *Annals of Nuclear Energy* **53**, 267 (2013).
- [13] S. Vanini, P. Calvini, P. Checchia, A. Rigoni Garola, J. Klinger, G. Zumerle, G. Bonomi, A. Donzella, and A. Zenoni, Muography of different structures using muon scattering and absorption algorithms, *Philosophical Transactions of the Royal Society A: Mathematical, Physical and Engineering Sciences* **377**, 20180051 (2018), publisher: Royal Society.
- [14] S. Procureur, Muon imaging: Principles, technologies and applications, *Nuclear Instruments and Methods in Physics Research Section A: Accelerators, Spectrometers, Detectors and Associated Equipment Radiation Imaging Techniques and Applications*, **878**, 169 (2018).
- [15] A. I. Titov, B. Kämpfer, and H. Takabe, Dimuon production by laser-wakefield accelerated electrons, *Physical Review Special Topics - Accelerators and Beams* **12**, 111301 (2009), publisher: American Physical Society.
- [16] B. S. Rao, J. H. Jeon, H. T. Kim, and C. H. Nam, Bright muon source driven by GeV electron beams from a compact laser wakefield accelerator, *Plasma Physics and Controlled Fusion* **60**, 095002 (2018), publisher: IOP Publishing.
- [17] L. Calvin, P. Tomassini, D. Doria, D. Martello, R. M. Deas, and G. Sarri, Laser-driven muon production for material inspection and imaging, *Frontiers in Physics* **11**, 10.3389/fphy.2023.1177486 (2023), publisher: Frontiers.
- [18] C. Aniculaesei, T. Ha, S. Yoffe, L. Labun, S. Milton, E. McCary, M. M. Spinks, H. J. Quevedo, O. Z. Labun, R. Sain, A. Hannasch, R. Zgadzaj, I. Pagano, J. A. Franco-Altamirano, M. L. Ringuette, E. Gaul, S. V. Luedtke, G. Tiwari, B. Ersfeld, E. Brunetti, H. Ruhl, T. Ditmire, S. Bruce, M. E. Donovan, M. C. Downer, D. A. Jaroszynski, and B. M. Hegelich, The acceleration of a high-charge electron bunch to 10 GeV in a 10-cm nanoparticle-assisted wakefield accelerator, *Matter and Radiation at Extremes* **9**, 014001 (2023).
- [19] J. Faure, Y. Glinec, A. Pukhov, S. Kiselev, S. Gordienko, E. Lefebvre, J.-P. Rousseau, F. Burgy, and V. Malka, A laser-plasma accelerator producing monoenergetic electron beams, *Nature* **431**, 541 (2004), number: 7008 Publisher: Nature Publishing Group.
- [20] C. G. R. Geddes, C. Toth, J. van Tilborg, E. Esarey, C. B. Schroeder, D. Bruhwiler, C. Nieter, J. Cary, and W. P. Leemans, High-quality electron beams from a laser wakefield accelerator using plasma-channel guiding, *Nature* **431**, 538 (2004), number: 7008 Publisher: Nature Publishing Group.
- [21] W. Leemans, A. Gonsalves, H.-S. Mao, K. Nakamura, C. Benedetti, C. Schroeder, C. Tóth, J. Daniels, D. Mittelberger, S. Bulanov, J.-L. Vay, C. Geddes, and E. Esarey, Multi-GeV Electron Beams from Capillary-Discharge-Guided Subpetawatt Laser Pulses in the Self-Trapping Regime, *Physical Review Letters* **113**, 245002 (2014), publisher: American Physical Society.
- [22] S. P. D. Mangles, C. D. Murphy, Z. Najmudin, A. G. R. Thomas, J. L. Collier, A. E. Dangor, E. J. Divall, P. S. Foster, J. G. Gallacher, C. J. Hooker, D. A. Jaroszynski, A. J. Langley, W. B. Mori, P. A. Norreys, F. S. Tsung, R. Viskup, B. R. Walton, and K. Krushelnick, Monoenergetic beams of relativistic electrons from intense laser-plasma interactions, *Nature* **431**, 535 (2004), number: 7008 Publisher: Nature Publishing Group.
- [23] X. Wang, R. Zgadzaj, N. Fazel, Z. Li, S. A. Yi, X. Zhang, W. Henderson, Y.-Y. Chang, R. Korzekwa, H.-E. Tsai, C.-H. Pai, H. Quevedo, G. Dyer, E. Gaul, M. Martinez, A. C. Bernstein, T. Borger, M. Spinks, M. Donovan, V. Khudik, G. Shvets, T. Ditmire, and M. C. Downer, Quasi-monoenergetic laser-plasma acceleration of electrons to 2 GeV, *Nature Communications* **4**, 1988 (2013), number: 1 Publisher: Nature Publishing Group.
- [24] W. Wang, W. Li, J. Liu, Z. Zhang, R. Qi, C. Yu, J. Liu, M. Fang, Z. Qin, C. Wang, Y. Xu, F. Wu, Y. Leng, R. Li, and Z. Xu, High-Brightness High-Energy Electron Beams from a Laser Wakefield Accelerator via Energy Chirp Control, *Physical Review Letters* **117**, 124801 (2016), publisher: American Physical Society.
- [25] A. Gonsalves, K. Nakamura, J. Daniels, C. Benedetti, C. Pieronek, T. de Raadt, S. Steinke, J. Bin, S. Bulanov, J. van Tilborg, C. Geddes, C. Schroeder, C. Tóth, E. Esarey, K. Swanson, L. Fan-Chiang, G. Bagdasarov, N. Bobrova, V. Gasilov, G. Korn, P. Satorov, and W. Leemans, Petawatt Laser Guiding and Electron Beam Acceleration to 8 GeV in a Laser-Heated Capillary Discharge Waveguide, *Physical Review Letters* **122**, 084801 (2019), publisher: American Physical Society.
- [26] B. Miao, J. Shrock, L. Feder, R. Hollinger, J. Morrison, R. Nedbailo, A. Picksley, H. Song, S. Wang, J. Rocca, and H. Milchberg, Multi-GeV Electron Bunches from an All-Optical Laser Wakefield Accelerator, *Physical Review X* **12**, 031038 (2022), publisher: American Physical Society.
- [27] A. Picksley, J. Stackhouse, C. Benedetti, K. Nakamura, H. E. Tsai, R. Li, B. Miao, J. E. Shrock, E. Rockafellow, H. M. Milchberg, C. B. Schroeder, J. v. Tilborg, E. Esarey, C. G. R. Geddes, and A. J. Gonsalves, Matched Guiding and Controlled Injection in Dark-Current-Free, 10-GeV-Class, Channel-Guided Laser Plasma Accelerators (2024), arXiv:2408.00740.
- [28] L. Kiani, T. Zhou, S.-W. Bahk, J. Bromage, D. Bruh-

- wiler, E. M. Campbell, Z. Chang, E. Chowdhury, M. Downer, Q. Du, E. Esarey, A. Galvanauskas, T. Galvin, C. Häfner, D. Hoffmann, C. Joshi, M. Kaskar, W. Lu, C. Menoni, M. Messerly, S. B. Mirov, M. Palmer, I. Pogorelsky, M. Polyanskiy, E. Power, B. Reagan, J. Rocca, J. Rothenberg, B. E. Schmidt, E. Sistrunk, T. Spinka, S. Tochitsky, N. Vafaie-Najafabadi, J. v. Tilborg, R. Wilcox, J. Zuegel, and C. Geddes, High average power ultrafast laser technologies for driving future advanced accelerators, *Journal of Instrumentation* **18** (08), T08006, publisher: IOP Publishing.
- [29] J. Jackson, *Classical electrodynamics*, Vol. 3 (Wiley New York etc., 1962).
- [30] A. W. Chao, K. H. Mess, and others, *Handbook of accelerator physics and engineering* (World scientific, 2013).
- [31] H. Bethe, W. Heitler, and P. A. M. Dirac, On the stopping of fast particles and on the creation of positive electrons, *Proceedings of the Royal Society of London. Series A, Containing Papers of a Mathematical and Physical Character* **146**, 83 (1997), publisher: Royal Society.
- [32] S. Agostinelli, J. Allison, K. Amako, J. Apostolakis, H. Araujo, P. Arce, M. Asai, D. Axen, S. Banerjee, G. Barrand, F. Behner, L. Bellagamba, J. Boudreau, L. Broglia, A. Brunengo, H. Burkhardt, S. Chauvie, J. Chuma, R. Chytracsek, G. Cooperman, G. Cosmo, P. Degtyarenko, A. Dell'Acqua, G. Depaola, D. Dietrich, R. Enami, A. Feliciello, C. Ferguson, H. Fesefeldt, G. Folger, F. Foppiano, A. Forti, S. Garelli, S. Giani, R. Giannitrapani, D. Gibin, J. J. Gómez Cadenas, I. González, G. Gracia Abril, G. Greeniaus, W. Greiner, V. Grichine, A. Grossheim, S. Guatelli, P. Gumplinger, R. Hamatsu, K. Hashimoto, H. Hasui, A. Heikkinen, A. Howard, V. Ivanchenko, A. Johnson, F. W. Jones, J. Kallenbach, N. Kanaya, M. Kawabata, Y. Kawabata, M. Kawaguti, S. Kelner, P. Kent, A. Kimura, T. Kodama, R. Kokoulin, M. Kossov, H. Kurashige, E. Lamanna, T. Lampén, V. Lara, V. Lefebvre, F. Lei, M. Liendl, W. Lockman, F. Longo, S. Magni, M. Maire, E. Medernach, K. Minamimoto, P. Mora de Freitas, Y. Morita, K. Murakami, M. Nagamatu, R. Nartallo, P. Nieminen, T. Nishimura, K. Ohtsubo, M. Okamura, S. O'Neale, Y. Oohata, K. Paech, J. Perl, A. Pfeiffer, M. G. Pia, F. Ranjard, A. Rybin, S. Sadilov, E. Di Salvo, G. Santin, T. Sasaki, N. Savvas, Y. Sawada, S. Scherer, S. Sei, V. Sirotenko, D. Smith, N. Starkov, H. Stoecker, J. Sulkimo, M. Takahata, S. Tanaka, E. Tcherniaev, E. Safai Tehrani, M. Tropeano, P. Truscott, H. Uno, L. Urban, P. Urban, M. Verderi, A. Walkden, W. Wander, H. Weber, J. P. Wellisch, T. Wenaus, D. C. Williams, D. Wright, T. Yamada, H. Yoshida, and D. Zschiesche, Geant4—a simulation toolkit, *Nuclear Instruments and Methods in Physics Research Section A: Accelerators, Spectrometers, Detectors and Associated Equipment* **506**, 250 (2003).
- [33] J. Allison, K. Amako, J. Apostolakis, H. Araujo, P. Arce Dubois, M. Asai, G. Barrand, R. Capra, S. Chauvie, R. Chytracsek, G. Cirrone, G. Cooperman, G. Cosmo, G. Cuttone, G. Daquino, M. Donszelmann, M. Dreschel, G. Folger, F. Foppiano, J. Generowicz, V. Grichine, S. Guatelli, P. Gumplinger, A. Heikkinen, I. Hrivnacova, A. Howard, S. Incerti, V. Ivanchenko, T. Johnson, F. Jones, T. Koi, R. Kokoulin, M. Kossov, H. Kurashige, V. Lara, S. Larsson, F. Lei, O. Link, F. Longo, M. Maire, A. Mantero, B. Mascialino, I. McLaren, P. Mendez Lorenzo, K. Minamimoto, K. Murakami, P. Nieminen, L. Pandola, S. Parlati, L. Peralta, J. Perl, A. Pfeiffer, M. Pia, A. Ribon, P. Rodrigues, G. Russo, S. Sadilov, G. Santin, T. Sasaki, D. Smith, N. Starkov, S. Tanaka, E. Tcherniaev, B. Tome, A. Trindade, P. Truscott, L. Urban, M. Verderi, A. Walkden, J. Wellisch, D. Williams, D. Wright, and H. Yoshida, Geant4 developments and applications, *IEEE Transactions on Nuclear Science* **53**, 270 (2006).
- [34] J. Allison, K. Amako, J. Apostolakis, P. Arce, M. Asai, T. Aso, E. Bagli, A. Bagulya, S. Banerjee, G. Barrand, B. R. Beck, A. G. Bogdanov, D. Brandt, J. M. C. Brown, H. Burkhardt, P. Canal, D. Cano-Ott, S. Chauvie, K. Cho, G. A. P. Cirrone, G. Cooperman, M. A. Cortés-Giraldo, G. Cosmo, G. Cuttone, G. Depaola, L. Desorgher, X. Dong, A. Dotti, V. D. Elvira, G. Folger, Z. Francis, A. Galoyan, L. Garnier, M. Gayer, K. L. Genser, V. M. Grichine, S. Guatelli, P. Guèye, P. Gumplinger, A. S. Howard, I. Hrivnáčová, S. Hwang, S. Incerti, A. Ivanchenko, V. N. Ivanchenko, F. W. Jones, S. Y. Jun, P. Kaitaniemi, N. Karakatsanis, M. Karamitros, M. Kelsey, A. Kimura, T. Koi, H. Kurashige, A. Lechner, S. B. Lee, F. Longo, M. Maire, D. Mancusi, A. Mantero, E. Mendoza, B. Morgan, K. Murakami, T. Nikitina, L. Pandola, P. Paprocki, J. Perl, I. Petrović, M. G. Pia, W. Pokorski, J. M. Quesada, M. Raine, M. A. Reis, A. Ribon, A. Ristić Fira, F. Romano, G. Russo, G. Santin, T. Sasaki, D. Sawkey, J. I. Shin, I. I. Strakovsky, A. Taborda, S. Tanaka, B. Tomé, T. Toshito, H. N. Tran, P. R. Truscott, L. Urban, V. Uzhinsky, J. M. Verbeke, M. Verderi, B. L. Wendt, H. Wenzel, D. H. Wright, D. M. Wright, T. Yamashita, J. Yarba, and H. Yoshida, Recent developments in Geant4, *Nuclear Instruments and Methods in Physics Research Section A: Accelerators, Spectrometers, Detectors and Associated Equipment* **835**, 186 (2016).
- [35] K. Nakamura, H.-S. Mao, A. J. Gonsalves, H. Vincenti, D. E. Mittelberger, J. Daniels, A. Magana, C. Toth, and W. P. Leemans, Diagnostics, control and performance parameters for the bella high repetition rate petawatt class laser, *IEEE Journal of Quantum Electronics* **53**, 1 (2017).
- [36] R. J. Shalloo, C. Arran, L. Corner, J. Holloway, J. Jonnerby, R. Walczak, H. M. Milchberg, and S. M. Hooker, Hydrodynamic optical-field-ionized plasma channels, *Physical Review E* **97**, 053203 (2018), publisher: American Physical Society.
- [37] L. Feder, B. Miao, J. E. Shrock, A. Goffin, and H. M. Milchberg, Self-waveguiding of relativistic laser pulses in neutral gas channels, *Physical Review Research* **2**, 043173 (2020), publisher: American Physical Society.
- [38] A. Picksley, A. Alejo, R. J. Shalloo, C. Arran, A. von Boetticher, L. Corner, J. A. Holloway, J. Jonnerby, O. Jakobsson, C. Thornton, R. Walczak, and S. M. Hooker, Meter-scale conditioned hydrodynamic optical-field-ionized plasma channels, *Physical Review E* **102**, 053201 (2020), publisher: American Physical Society.
- [39] D. E. Groom, N. V. Mokhov, and S. I. Striganov, Muon stopping power and range tables 10 MeV–100 TeV, *Atomic Data and Nuclear Data Tables* **78**, 183 (2001).
- [40] R. Frühwirth and M. Regler, On the quantitative modelling of core and tails of multiple scattering by Gaussian mixtures, *Nuclear Instruments and Methods in Physics*

Research Section A: Accelerators, Spectrometers, Detectors and Associated Equipment **456**, 369 (2001).

[41] H. A. Bethe, Moliere's Theory of Multiple Scattering, *Physical Review* **89**, 1256 (1953), publisher: American Physical Society.

[42] L. Dahing, R. Yahya, R. Yahya, and H. Hassan, Non de-

structive multi elemental analysis using prompt gamma neutron activation analysis techniques: Preliminary results for concrete sample, *AIP Conference Proceedings* **1614**, 20 (2014).